



ALICE-PUBLIC-2018-013

Expression of Interest for an ALICE ITS Upgrade in LS3

ALICE Collaboration, CERN, Geneva, Switzerland

Abstract

Recent innovations in the field of silicon imaging technology for consumer applications open extraordinary opportunities for new detector concepts, and hence offer strongly improved physics scope. This document presents a proposal for the construction of a novel vertex detector consisting of curved wafer-scale ultra-thin silicon sensors arranged in perfectly cylindrical layers, featuring an unprecedented low material budget of $0.05\% X_0$ per layer, with the innermost layer positioned at only 18 mm radial distance from the interaction point. This new vertex detector is planned to be installed during the LHC LS3 to replace the innermost three layers of the ALICE Inner Tracking System. It will provide a large reduction of the material budget in the region close to the interaction point and a large improvement of the tracking precision and efficiency at low transverse momentum. The combination of these two improvements will lead to a significant advancement in the measurement of low momentum charmed hadrons and low-mass dielectrons in heavy-ion collisions at the LHC, which are among the main objectives of the ALICE physics programme in the next decade.

Geneva, Switzerland
January 6, 2019

Contents

1	Introduction	3
2	Upgrade Concept	4
2.1	The ITS2 Inner Barrel	4
2.2	An Ultra Lightweight Vertex Detector	5
2.3	Development of a Novel Wafer-scale Curved Sensor	7
3	Detector Layout, Implementation and Main Parameters	9
3.1	Mechanical Structure	9
3.2	Cooling	11
3.3	System Integration	11
4	Detector Performance	12
4.1	Particle Rates and Radiation Load	12
4.2	Tracking Performance	13
5	Physics Performance	15
5.1	Measurement of Λ_c Production	15
5.2	Measurement of Thermal Dielectrons	17
6	Project Cost Estimate	20

1 Introduction

ALICE is preparing a major upgrade of its detector [1, 2, 3, 4, 5, 6] to be installed during the second long LHC shutdown (LS2). The main objective is to increase the readout capabilities to allow the readout and recording of Pb–Pb minimum bias events at rates in excess of 50 kHz, the expected Pb–Pb interaction rate at the LHC after LS2. This increase in readout speed, together with the deployment of a new data acquisition system that will allow recording all collisions, will imply an increase by about two orders of magnitude in the collectible minimum-bias statistics compared to the present ALICE set-up. One of the key components of the LS2 upgrade programme is the replacement of the current Inner Tracking System (ITS) with an entirely new one (ITS2) with increased vertexing and tracking performance, especially for particles with low transverse momentum ($p_T < 1 \text{ GeV}/c$). The new ITS consists of seven approximately-cylindrical detector layers based on CMOS Monolithic Active Pixel Sensors (MAPS) with the sensor matrix and readout integrated in a single chip, named ALPIDE (ALice PIxel DEtector), covering a 10 m^2 area with about 12.5 billion pixels.

ALPIDE is the result of an intensive R&D effort carried out by ALICE in the past eight years which has led to a quantum leap in the field of MAPS for single-particle detection, reaching unprecedented performance in terms of signal/noise ratio, spatial resolution, material budget and readout speed. Yet, there is still a lot that can be done to further improve MAPS for high-energy physics detectors by fully exploiting the rapid progress that this technology is making in the field of imaging for consumer applications. One of the features offered recently by CMOS imaging sensor technologies, called *stitching*, will allow developing a new generation of large size MAPS with an area of up to $14 \text{ cm} \times 14 \text{ cm}$. Moreover, the reduction of the sensor thickness to values of about $20 - 40 \mu\text{m}$ will open the possibility of exploiting the flexible nature of silicon to implement large-area curved sensors. In this way, it will become possible to build a cylindrical layer of silicon-only sensors, with a further significant reduction of the material thickness.

This document presents a proposal for the construction of a new vertex detector consisting of three cylindrical layers based on curved wafer-scale stitched sensors, featuring a material budget of $0.05 \% X_0$ per layer, with the first layer positioned at a radial distance from the interaction point of 18 mm. This new vertex detector will be installed during LS3 to replace the three innermost layers of the ITS2. The plan is to install also a new beam-pipe with smaller radius (inner radius 16 mm) and thickness (500 μm), which will replace the beam-pipe that will be installed in LS2 as part of the ALICE phase I upgrade (inner radius of 18.2 mm and thickness of 800 μm). With the first detection layer closer to the interaction point (from 23 mm to 18 mm) and a reduction of the material budget close to the interaction point by a factor of six, the new vertex detector will significantly improve the tracking precision and efficiency at low p_T . The improvement of the vertexing performance and the reduction of material budget will have a dramatic impact on the measurement of charmed hadrons at low transverse momentum as well as on the measurement of low-mass and low p_T dielectrons.

The document presents the technical aspects of the proposed development and the required R&D efforts in Section 2. The detector geometry and physical layout are presented in Section 3, while the projected detector performance and physics performance are discussed in Section 4 and Section 5, respectively. Section 6 provides a first estimate of the required resources and the development timeline.

2 Upgrade Concept

2.1 The ITS2 Inner Barrel

The design of the ITS2 is conceived as a two-barrel structure: the Inner Barrel (IB), formed by Layers 0 to 2, and the Outer Barrel (OB), formed by Layers 3 to 6. The three Layers of the IB are also referred to as the Inner Layers, while, for the OB, Layers 3 and 4 are referred to as Middle Layers and Layers 5 and 6 as Outer Layers. In the azimuthal direction, each Layer is segmented in elements called Staves. The Stave, which extends over the whole length of the respective Layer, is the basic building block of the detector. The Stave contains all structural and functional components, thus making it the smallest operable part of the detector.

Since one of the main motivations of this upgrade proposal is the reduction of the material budget of the Inner Layers, let us begin by briefly introducing the layout of the ITS2 Inner Barrel and discussing its material budget distribution. The three Inner Layers are built with identical Staves, which are based on the following elements:

- **Space Frame:** a carbon fibre support structure providing the mechanical support and the necessary stiffness;
- **Cold Plate:** a sheet of high thermal-conductivity carbon fibre with embedded polyimide cooling pipes, which is integrated into the Space Frame. The Cold Plate is in thermal contact with the Pixel Chips to remove the generated heat.
- **Hybrid Integrated Circuit (HIC):** an assembly consisting of a polyimide Flexible Printed Circuit (FPC) onto which the Pixel Chips and some passive components are bonded.

Each IB Stave is instrumented with one HIC, which consists of nine Pixel Chips in a row connected to the FPC, covering an active area of $15\text{ mm} \times 270.8\text{ mm}$ including $100\text{ }\mu\text{m}$ gaps between adjacent chips along the longitudinal direction (z). The interconnection between Pixel Chips and FPC is implemented via conventional aluminum wedge wire bonding. The HIC is glued to the Cold Plate with the Pixel Chips facing it in order to maximise the cooling efficiency. A schematic drawing and a photograph of the IB Stave are shown in Figs. 1 and 2, respectively. An extension of the FPC, not shown in the figure, connects the Stave to a patch panel that is served by the electrical services entering the detector only from one side.

The production of the IB Staves is nearly completed and a photograph of the the three layers composing a half-barrel is shown in Fig. 3. Figure 4 shows the azimuthal distribution (averaged over the full barrel longitudinal length) of the material of Layer 0 traversed by particles at $\eta = 0$. Adjacent Staves are partially overlapping to ensure detector hermeticity. The highest peaks correspond to the overlap of the reinforced structures along the edges of the Space Frame, which guarantee the required stiffness, while the narrow spikes correspond to the reinforcement of the upper vertex. The peaks around $0.5\% X_0$ are due to the polyimide cooling pipes embedded in the Cold Plate, which have an inner diameter of 1.024 mm and a wall thickness of $25\text{ }\mu\text{m}$ and are fully filled with water during the operation of the detector. The average value ($0.358\% X_0$) is unprecedentedly low, which is of crucial importance to achieve high impact parameter resolution at low transverse momentum. The ITS2 is thus one of the cornerstones of the ALICE upgrade. In the following, we propose a further considerable improvement.

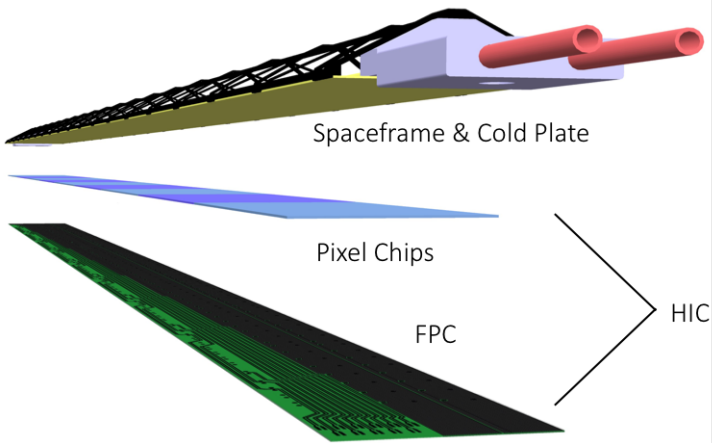


Figure 1: Schematic layout of the ITS2 Inner Barrel Stave. Nine pixel sensors are flip-chip mounted on a flexible printed circuit (FPC) to form a hybrid integrated circuit (HIC). The HIC is glued on a carbon fibre support structure (Spaceframe), which integrates a water cooling circuit (Cold Plate).



Figure 2: Photograph of a production sample of the ITS2 Inner Barrel Stave.

2.2 An Ultra Lightweight Vertex Detector

Can the material thickness of the Inner Layers be further reduced? The material budget breakdown of the ITS2 shows very clearly that the silicon sensor, which has a thickness of $50\ \mu\text{m}$ and ideally is the only component that would be needed in the detector acceptance, contributes only 15% to the total. The rest is due to the material of the electrical substrate (FPC), which represents the main contribution (50% including the passive components and the glue), to the cooling circuit (20%) and to the carbon spaceframe (15%). It is clear that, in order to significantly improve on the material budget, the electrical, mechanical and cooling material have to be attacked next. A natural question in this context is whether it is at all possible to envisage a detector that would completely do away with an electrical substrate and an active cooling circuit in the detector acceptance.

The electrical substrate is the flexible printed circuit that distributes the supply and bias voltages as well as the data and control signals to the pixel sensors. In standard CMOS manufacturing, the maximum size of a chip is limited to the reticle area defined by the field of view of the photolithographic process, which is typically a few centimeters in both directions. For this reason, the Stave surface is covered by tiling several sensors. However, a recent technology,

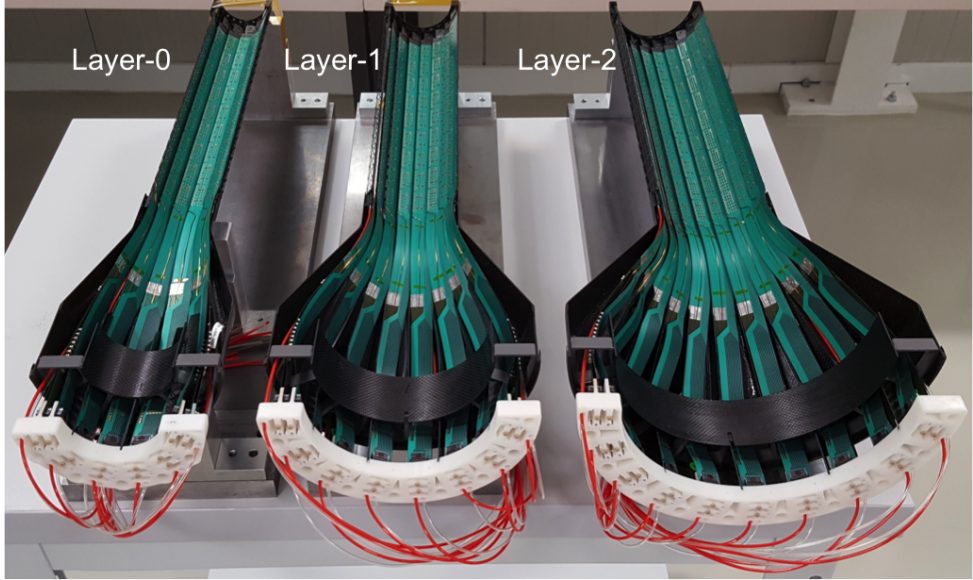


Figure 3: Photograph of the ITS2 IB half-layers (Layer-0, Layer-1 and Layer-2).

called stitching, allows fabricating sensors of arbitrary dimensions, the only limit being the size of the wafer. As described in the next section, this opens the possibility of fabricating a pixel sensor with the dimension of an entire stave. The distribution of power and electrical signals could then be done entirely inside the silicon chip and the electrical substrate would terminate close to the chip edge, where the interconnections to the chip would be realized.

Concerning the elimination of the material associated with the cooling circuit, the possibility of using a low-speed ($< 2 \text{ m s}^{-1}$) air flow to remove the heat produced by the ITS Inner Layers by convection, in combination with peripheral liquid cooling, was studied already in the context of the R&D for the ITS2. It was experimentally demonstrated that this is a viable option for sensors with a power density below 20 mW cm^{-2} [7]. In this regard, it should be noticed that the higher the air flow, the stiffer the mechanical support structure has to be, in order to keep the vibrations of the sensor, caused by the air flow, smaller than the intrinsic spatial resolution. For large values of the sensor power density, therefore, the reduction of material obtained by replacing an active cooling circuit with an air flow can be offset by an increase of material needed to make the mechanical support structure sufficiently stable.

The ALPIDE chip contains approximately 5×10^5 pixels, each measuring about $27 \mu\text{m} \times 29 \mu\text{m}$, arranged in 512 rows and 1024 columns, for a total active area of $30 \text{ mm} \times 15 \text{ mm}$. The total power consumption is 180 mW, which corresponds to a power density of about 40 mW cm^{-2} . However, most of this power (about 150 mW) is dissipated by the digital interface circuitry and the high-speed output data links, which are located in a small area of about $30 \text{ mm} \times 1.5 \text{ mm}$ close to one edge of the chip. Only about a sixth of the total power is dissipated in the pixel matrix, which corresponds to a power density of about 7 mW cm^{-2} . This would be well within the range for which air cooling represents a viable and effective solution. Thus, the question arises: can we put the pixel sensor digital periphery at the edge of the detector? Again, this would be possible if the pixel sensor had the dimensions of a stave.

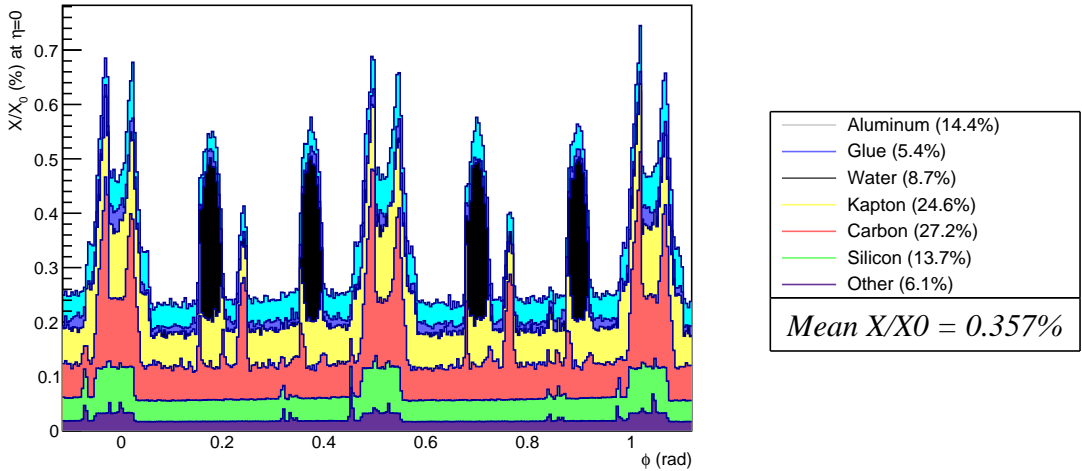


Figure 4: Azimuthal distribution (averaged over the full barrel length) of the material budget of ITS2 Layer 0. The angular interval in the figure corresponds to two staves, with $\varphi = 0$ on the horizontal plane, where two staves from the upper and lower half barrels partly overlap.

2.3 Development of a Novel Wafer-scale Curved Sensor

The construction of a silicon pixel tracker based on large-area sensors excluding from the detector acceptance all services and mechanical support structures would represent a real breakthrough. As we have seen in the previous section, at present small sensors are mounted edge-to-edge on top of a flexible PCB module that provides the power distribution and data bus. The key new idea is to make use of the stitching technology to replace such a module with a single large sensor, where power distribution is managed internally, confining to the sensor edge the interconnections to the outside world.

The largest field of view that is used in the photolithographic steps needed to make any CMOS circuitry, including imaging sensors, defines the reticle size, normally of a few centimeters in both directions. In standard CMOS circuit manufacturing, the reticle is just stepped and repeated across the wafers to create multiple identical images of the same circuit or group of circuits. The reticle area defines the maximum size of the chip. Stitching is a technology that allows the fabrication of an image sensor that is larger than the field of view of the lithographic equipment. In this technology, the reticles which fit into the field of view of that equipment are placed on the wafer with high precision, achieving a tiny but well defined overlap. In this way, wafer-scale sensors can be manufactured. As a qualitative example, Fig. 5 shows a wafer-scale imaging sensor chip for X-Ray applications of size 139.2 mm \times 120 mm produced by stitching with the Tower Semiconductor 0.18/0.35 μm dual-gate process with 200 mm wafers [8].

The current proposal is to develop a new circuit, schematically represented in Fig. 6, of size 15 mm \times 140 mm, which is about half of the stave length. The columns run along the short side of the sensor, and have the same length as in the ALPIDE sensor. Data are extracted from the matrix as in the ALPIDE chip with hit-driven circuitry based on a priority-encoder addressing scheme [9]. Groups of 16 double columns are read out sequentially, but in principle all of them could be read out in parallel. Data are transmitted from the bottom of the columns along one long side of the sensor to the periphery, as indicated by the black arrow at the bottom of Fig. 6. The periphery, shown on the left part of the sensor in Fig. 6, contains the control logic

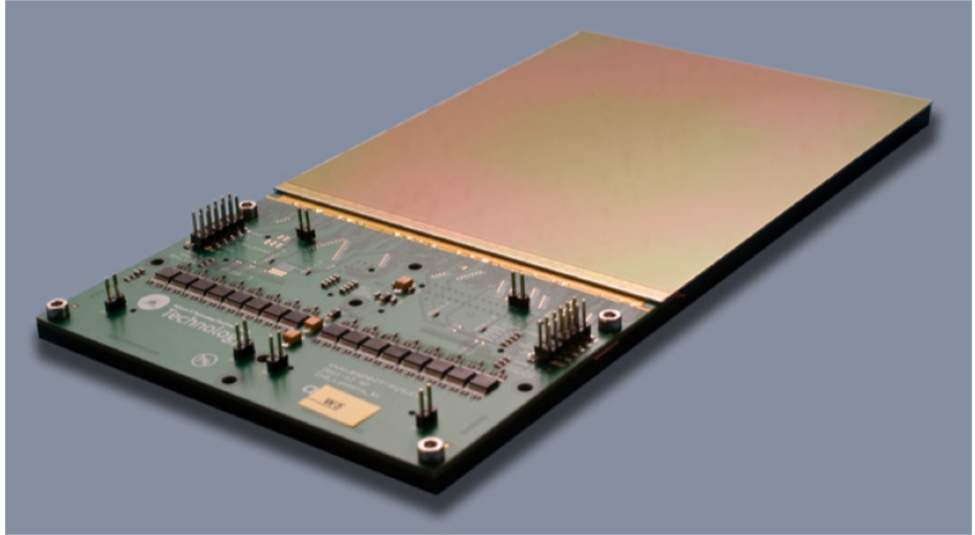


Figure 5: Photograph of a stitched sensor chip for X-Ray applications of size $139.2\text{ mm} \times 120\text{ mm}$ produced by stitching with the Tower Semiconductor 0.18/0.35 μm dual-gate process with 200 mm wafers.

to steer the priority encoders, the interface for the configuration of the chip and the serial data transmitters. The required memory buffers and serial transmitters will be properly dimensioned to match the requirements in terms of data throughput. Since the chip periphery is outside the detector acceptance, there is no particular constraint on the size of the periphery that will be adjusted on the basis of the requirements.

The distribution of power inside the sensor also has to be considered carefully. In the ALPIDE, there are two metal meshes with pads all over the chip surface. In principle, the technology offers the possibility to add a metal layer (called re-distribution layer) underneath the chip passivation layer. The meshes or distribution layer are then connected to the power pads located in the chip periphery. A flexible PCB, placed only under the digital periphery of the chip, will provide power to the sensor.

The large sensor will be thinned to values of about $20\text{ }\mu\text{m}$ to $40\text{ }\mu\text{m}$, which correspond to a radiation thickness of 0.2% to $0.4\% X_0$, and its surface finished with plasma polishing to release mechanical stress. The possibility to bend and operate ultra-thin sensors to a curvature radius of about 20 mm seems very promising [10], opening the way to the construction of a silicon-only cylindrical layer.

A 200 mm wafer can contain a square matrix of about $14\text{ cm} \times 14\text{ cm}$, or about 200 cm^2 . A 2D stitched wafer-scale sensor can be obtained replicating the 1D stitched sensor chip several times along the periphery side. Such a sensor chip, containing about 5000×5000 pixels, would also provide radically new options for the construction of a future very large-area silicon tracker.

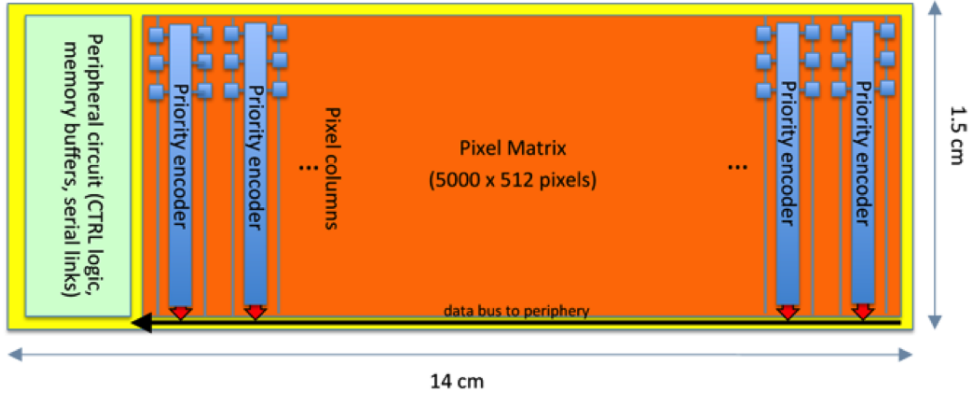


Figure 6: Diagram of stitched sensor in one direction (horizontal and vertical dimensions not to scale). Stitching in the vertical direction is also possible.

3 Detector Layout, Implementation and Main Parameters

3.1 Mechanical Structure

The ITS3 will consist of two separate barrels, referred to as Inner Barrel and Outer Barrel. The Outer Barrel, containing the four outermost layers (Layer 3 to Layer 6), will be that of ITS2. A completely new Inner Barrel, consisting of the three innermost layers (Layer 0 to Layer 2), will instead replace the current Inner Barrel of ITS2. The ITS3 IB will consist of two halves, named half-barrels, to allow the detector to be mounted around the beam pipe. Each half-barrel will consist of three half-layers. The half-layers are arranged inside the half-barrel as shown in Fig. 7. They have a truly (half-) cylindrical shape, with each half-layer segmented longitudinally (at $z = 0$) in two halves, named quarter-layers. Each quarter-layer consists of a single large pixel chip, which is curved to a cylindrical shape.

As shown in Fig. 8, the main structural components of the new Inner Barrel are the End-Wheels and the outer Cylindrical Structural Shell (CYSS), both made of Carbon Fibre Reinforced Plastic (CFRP) materials, and a series of ultra-lightweight half-wheel spacers, made of open cell carbon foam, which are inserted between layers to define their relative radial position.

The End-Wheels are connected to the CYSS, which provides the external supports for the three detection layers. Starting from the outermost layer (Layer 2), the half-layers are connected to the outer CYSS and to each other by means of the half-wheel spacers.

The quarter-layer consists of a single large chip. Its periphery and interface pads are all located on one edge, the one facing the A-side End-Wheel (see Fig. 8). At this edge, the chip is glued over a length of about 5 mm to a flexible printed circuit to which it is electrically interconnected using aluminum wedge wire bonding. The flexible printed circuit is based on polyimide, as dielectric, and aluminum, as conductor. The flexible printed circuit extends longitudinally from the chip edge through the End-Wheel until it reaches a patch panel located a few centimeters away, where interconnections to the electrical data cables and power cables are realized.

The basic principle for the half-barrel assembly, which is based on the use of the CYSS as exoskeleton, can be summarized as follows. A baseplate jig keeps the CYSS in place, providing a reference system for the assembly of the three half-layers. A second jig, mating the baseplate, is used to position the half-wheel carbon foam spacers, which are glued to the CYSS. A cylindrical vacuum chuck keeps the half-layer 2 curved to the nominal radius and, by mating

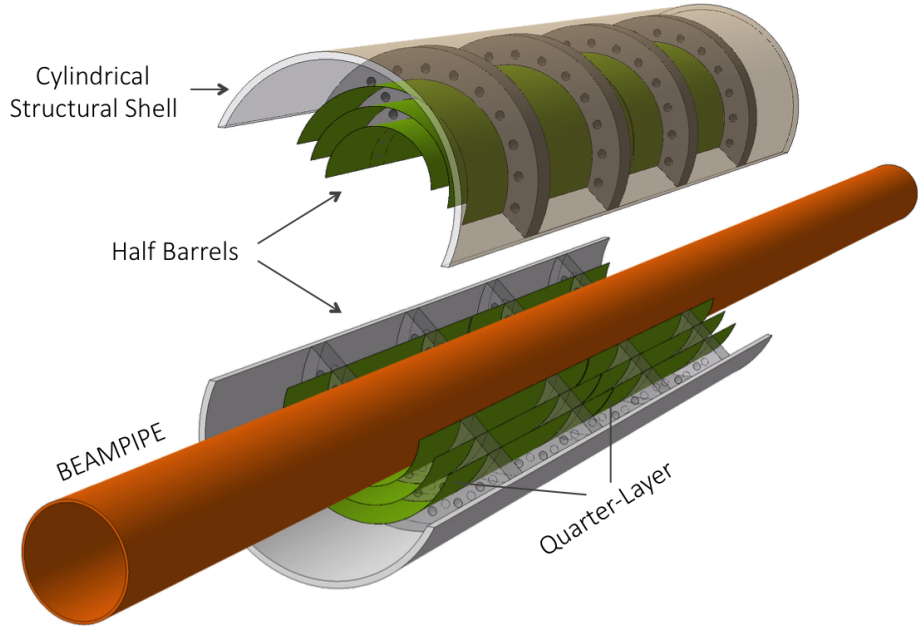


Figure 7: Layout of the ITS3 Inner Barrel. The figure shows the two half-barrels mounted around the beam pipe.

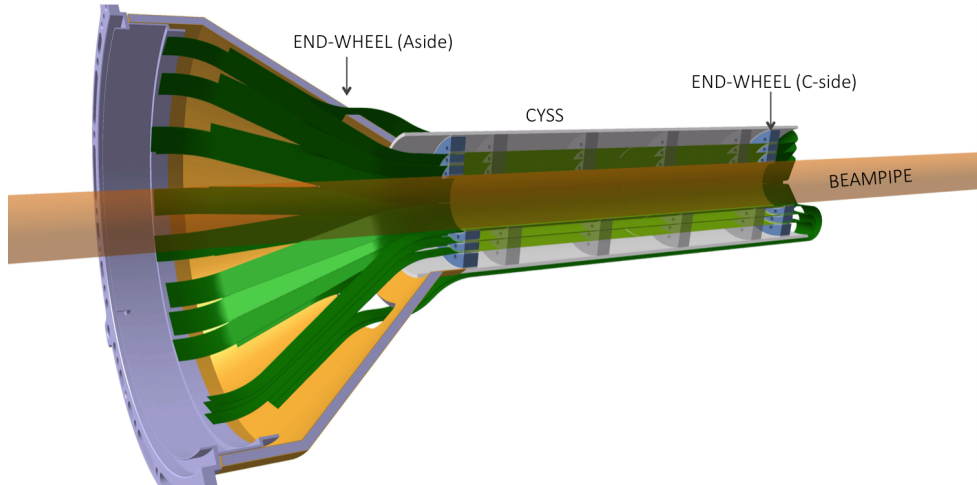


Figure 8: Layout of the ITS3 Inner Barrel. Two end-wheels and the CYSS provide precise position of the detector relative to the beampipe. On the C-side, the cables first exit from the C-side End-Wheel, then they are folded to the outside of the CYSS and routed towards the A-side.

the baseplate, brings it in position on the carbon foam spacers inside the CYSS. A thin layer of glue, at the interface, provides the mechanical fixation of the half-layer. The two spacers, positioned at the two edges of the half layer, provide the fixation interface for the 5mm wide area at the chip edge, where the mechanical and the electrical connection to the FPC are made . A second set of spacers is then glued to the internal surface of the half-layer 2. The same procedure is then repeated for half-layers 1 and 0, respectively, using their corresponding cylindrical vacuum chucks and carbon foam spacers with the appropriate curvature radii.

The main layout and geometrical parameters of the ITS3 Inner Barrel are summarized in Tab. 1

Table 1: Geometrical parameters of the upgraded ITS.

Beam pipe inner/outer radius (mm)	16.0/16.5		
IB Layer parameters	Layer 0	Layer 1	Layer 2
Radial position (mm)	18.0	24.0	30.0
Length (sensitive area) (mm)	270	270	270
Pseudo-rapidity coverage ^a	± 2.5	± 2.3	± 2.0
Active area (cm^2)	305	408	508
Pixel sensors dimensions (mm^2)	140×56.5	140×75.5	140×94
Number of pixel sensors / layer	4		
Pixel size (μm^2)	$O(30 \times 30)$		

^a The pseudorapidity coverage of the detector layers refers to tracks originating from a collision at the nominal interaction point ($z = 0$).

and are the basis for the detector and physics performance studies that are presented in Sections 4 and 5.

3.2 Cooling

The heat dissipated by the sensors is removed by convection through a forced airflow between the layers; in addition, the carbon foam rings in thermal contact with the sensors act as radiators reducing the thermal gradient along the layer. The enhancement of convective heat transfer due to the carbon foam rings results from the passage of the air through the open-interconnected void structure, which has an internal surface with an area to volume ratio as large as 5000 m^{-1} to 50000 m^{-1} . However, the complex internal structure of the foam could induce flow resistance and a relatively high air pressure drop. In order to reduce this pressure drop, a heat radiator with slots that open preferential flow paths in the carbon foams must be used.

A combination of excellent thermal conductivity with low density has made carbon foam materials prime candidates for use in modern heat exchangers. Materials such as KFOAM feature a thermal conductivity similar to that of aluminum at one-fifth of the density and with a coefficient of thermal expansion that is close to that of silicon. POCO HTC, which is a new porous graphite material specifically designed for high thermal performance, shows two-thirds of the thermal conductivity of copper at only one-tenth of the weight [11] [12]. During the design process, the airflow speed will be optimised to guarantee the thermal performance and mechanical stability by avoiding airflow-induced vibrations.

3.3 System Integration

The requirement to locate the first layer at a minimal distance from the beam pipe drives the design of the mechanical support structure. The integration scheme is similar to the one adopted for the ITS2, with the detector mechanically decoupled from the beam pipe and completely

supported by an extractable barrel (service barrel) which is fixed to the cage, as shown in Fig. 9.

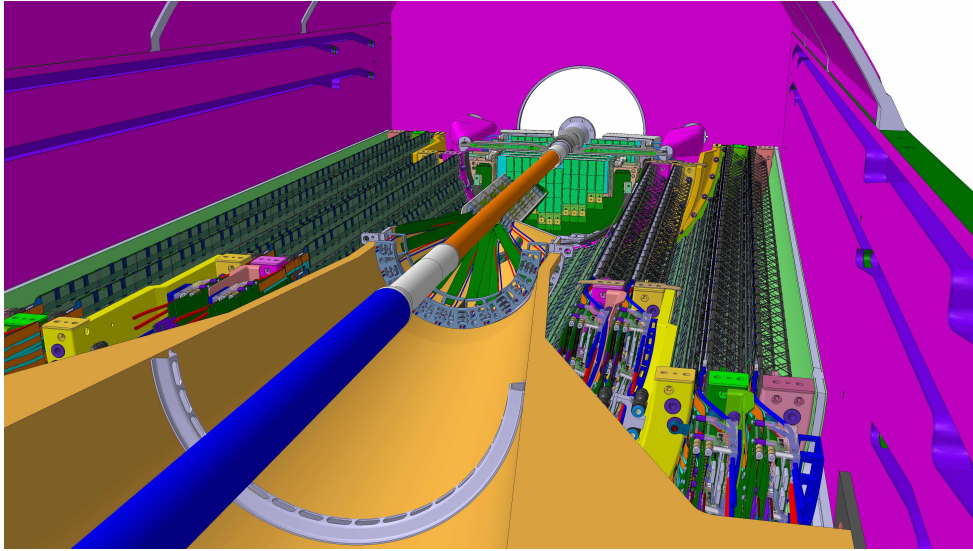


Figure 9: Layout of the ITS3 and integration of the Inner Barrel. The detector is mechanically decoupled from the beampipe and supported by the service barrel (yellow conical structure in the figure), which is fixed to the cage (magenta cylindrical structure in the figure).

The End-Wheels at the barrel extremities provide accurate positioning and fixation of the detector with respect to the beam pipe. The End-Wheels also provide a path for the services to exit the detector on both sides (ALICE A-side and C-side). On the A-side, the flexible printed circuit, connected to the quarter-layer at its edge, is entirely outside the sensitive volume, and extends to a patch panel on the service wheel, a few centimeters away from the End-Wheels, where the interconnections to power and data cables are made. On the C-side, instead, the cables first exit from the inside of the the IB trough the C-side End-Wheel, then they are folded to the outside of the CYSS and routed towards the A-side, where they enter to the inside of the End-Wheel, as shown in Fig. 8.

The routing of the services from the A-side End-Wheel to the patch panels off detector will follow the same design solutions adopted for the ITS2. It should also be noted that such an integration scheme, which is based on the same integration concept adopted for the ITS2, will allow a fast extraction of the ITS3.

4 Detector Performance

In this section, we discuss the improvement of the performance of the ALICE central tracker, in terms of tracking precision and efficiency, due to the installation of the ITS3. Before describing the simulations carried out for the study of the detector performance, we review the experimental conditions, in particular the particle flux and the radiation load.

4.1 Particle Rates and Radiation Load

Since the Inner Layers will be closer to the interaction point than in the case of the ITS2, the flux of particles crossing the innermost layer, and correspondingly the radiation load, will

Table 2: Expected maximum particle density in the layers of the ITS Inner Barrel.

Layer	Particle density (cm^{-2})			
	LS2 Upgrade		LS3 Upgrade	
	Hadronic ^a	QED electrons ^b	Hadronic ^a	QED electrons ^b
0	43	7	73	12
1	25	3	43	8
2	17	2	29	6

^a maximum particle density in central Pb–Pb collisions (including secondaries produced in material) for a magnetic field of 0.2 T.

^b for an integration time of 10 μs , an interaction rate of 50 kHz, a magnetic field of 0.2 T

increase. Table 2 summarises the expected maximum hit densities for primary and secondary charged particles. An additional contribution to the overall particle load comes from e^+e^- pairs generated by the electromagnetic interaction of the crossing ions. These will be referred to as QED electrons. This contribution depends on the detector integration time. The table lists the particle density for the Inner Barrel of the ITS3 and, for comparison, of the Inner Barrel of ITS2. The particle density at the location closer to the interaction point will increase by about 70%. However, owing to the high detector granularity, the hit occupancy (fraction of pixels with a particle hit) still remains rather low (1×10^{-3}) and well within the tracking capabilities of the ITS3. With such a hit density the innermost layer will see a particle flux of about 4 MHz cm^{-2} for a Pb–Pb interaction rate of 50 kHz, which is well within the rate capabilities of the ALPIDE sensor. The radiation load will also increase by 60–70%, but still remains well below $1 \times 10^{13} \text{ MeV } n_{\text{eq}}/\text{cm}^2$ (NIEL) and 10 kGy (TID), values for which the ALPIDE sensor was verified to fully preserve its performance.

4.2 Tracking Performance

The tracking performance has been studied using a Fast Monte Carlo Tool (FMCT), which is based on the same simulation methods and tools used for the LS2 upgrade studies. The tool accounts for multiple scattering, secondary interactions and detector occupancy, but ignores the particles’ energy loss in the beam pipe and in the detector. The FMCT provides accurate determination of the tracking resolution as a function of the detector configuration for both the spatial and the momentum components and a good estimate of the tracking efficiency. The FMCT has been used to optimise the layout of the detector in terms of number of layers, their radial positions, material budget and detector resolution with the same approach discussed in the Technical Design Report for the Upgrade of the ALICE Inner tracking System [1, Sec. 7.4].

An important measure of the achieved tracking precision is the track impact-parameter resolution, defined as the dispersion of the distribution of the Distance of Closest Approach (DCA) of the reconstructed (primary) tracks to the interaction vertex. It is the parameter that defines the capability of a vertex detector to separate secondary vertices of heavy-flavour decays from the interaction vertex. A comparison of the impact-parameter resolution of ITS2 and ITS3 is shown in Fig. 10 for pions at typical pseudorapidity $\eta = 0.5$. The solid lines show the resolution for

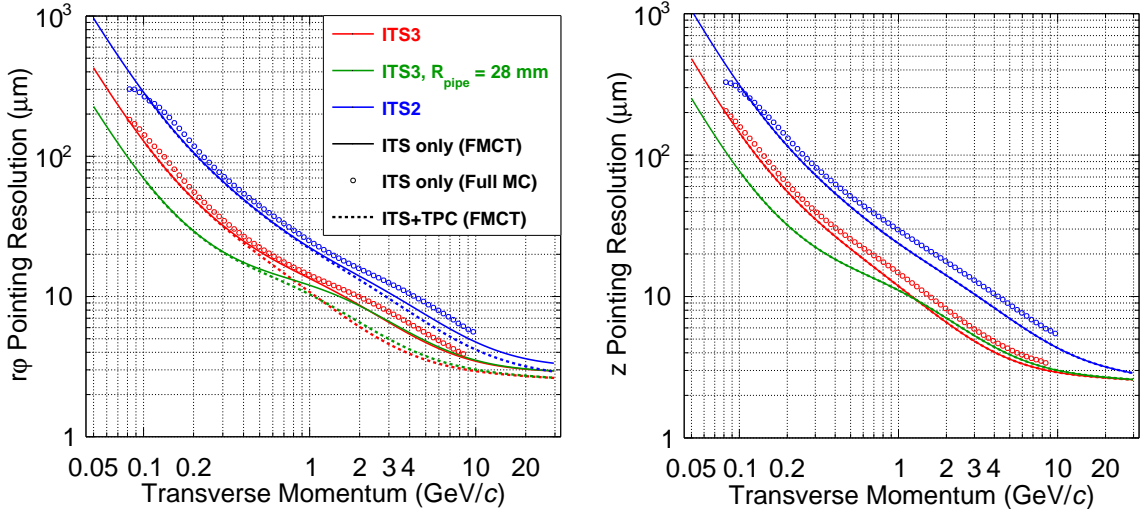


Figure 10: Impact parameter resolution for primary charged pions as function of the transverse momentum for the ITS2 upgrade (blue) and the ITS3 upgrade (red) in the transverse plane (left panel) and in the longitudinal direction (right panel). The green curves ($ITS3, R_{\text{pipe}} = 28 \text{ mm}$) refer to the detector configuration with the innermost two layers inside the vacuum chamber (see the text for further details). All solid lines show the results with FMCT and ITS only, all dashed lines show the results with FMCT and ITS+TPC, all open circles show the results with Full MC and ITS only.

tracks fitted in the seven ITS layers only, while the dashed lines show the resolution for tracks fitted in both the TPC and the ITS. For $p_T \simeq 1 \text{ GeV}/c$, the impact parameter resolution of ITS3 plus TPC is a factor of about two better than that of ITS2 plus TPC.

The resolutions for the ITS-only case were also estimated with a Full MC simulation setup, in which a simplified ITS3 inner barrel geometry was implemented within the ITS2 geometry in the ALICE software framework. In this simulation, pions were transported through the detector material using the GEANT3 package [13] and their trajectories were reconstructed using the Cellular Automaton ITS tracker [1]. The Full MC resolutions are shown by the circles for both ITS2 and ITS3 in Fig. 10 and are found to be very similar to those obtained with FMCT. The improvement factor from ITS2 to ITS3 is thus confirmed with the Full MC.

An alternative scenario in which the two innermost layers of the Inner Barrel are contained inside the beam vacuum chamber, while the third one is located outside of it at a radial distance of 1.5 mm from the outer wall, was also studied. In this configuration, the radii of the Inner Barrel layers remain the same as in the previous configuration, i.e. 18 mm, 24 mm and 30 mm, respectively, while the beam pipe has an inner radius of 28 mm. The performance with this configuration is also illustrated in Fig. 10. This scenario is evoked here to indicate that there is still some scope for improvement, which however would require a dedicated R&D effort. This option is not part of the upgrade proposal for LS3, and will not be discussed further in this document.

The left panel of Fig. 11 shows the track-finding efficiency in the environment of a single central Pb–Pb collision. It should be noted that the plot shows the efficiency only for "correct tracks", i.e. tracks that contain all clusters produced by the same particle, while at low p_T there will be a significant contribution from tracks with one or more clusters from other particles. The p_T

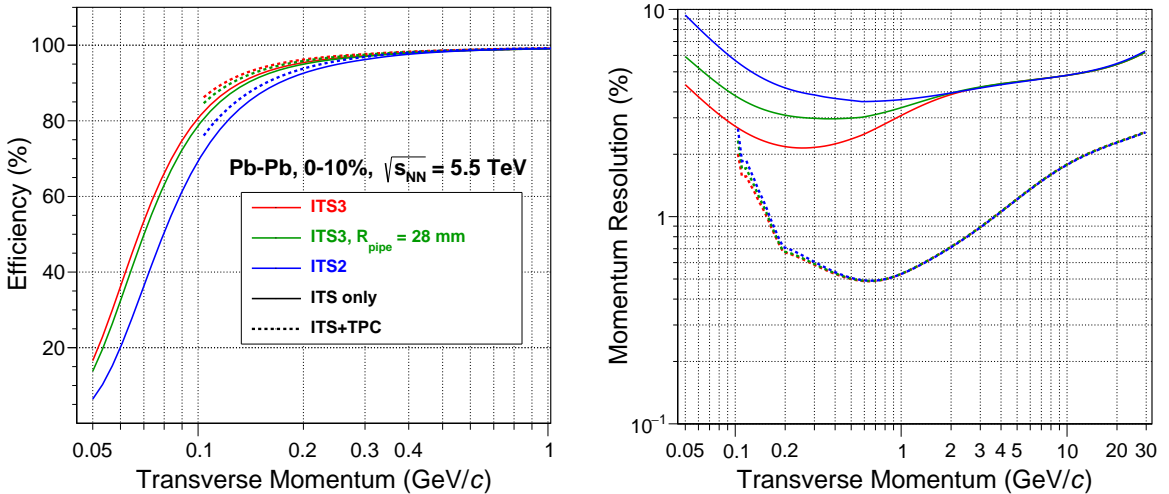


Figure 11: Track finding efficiency in central Pb–Pb collisions (left panel) and transverse momentum relative resolution (right panel) in the ITS-only (solid lines) and ITS–TPC combined (dashed) reconstruction modes as function of transverse momentum for the ITS2 and two different ITS3 detector configurations (see text for the details). All solid lines show the results with FMCT and ITS only, all dashed lines show the results with FMCT and ITS+TPC.

resolution of the ITS3, shown on the right panel of Fig. 11, benefits significantly from the lower material budget of the Inner Barrel in the ITS-only mode. In the ITS–TPC combined tracking mode, at p_T below 0.5 GeV/ c , the ITS3 configuration essentially gives the same p_T resolution as ITS2.

5 Physics Performance

The improved vertex resolution will be beneficial for the measurement at low transverse momentum of many of the observables studied by ALICE. The improved impact parameter resolution and the reduced material budget of the proposed layout will significantly extend the physics capability for the study of heavy-flavour production, notably in the baryon sector, and for the study of low-mass dielectrons, two of the main objectives of the ALICE physics programme in the next decade. In this section the Λ_c and thermal dielectron measurements will be presented as benchmarks to quantitatively demonstrate the impact of the proposed upgrade.

5.1 Measurement of Λ_c Production

The measurement of the production yields and flow of charm and beauty baryons is of particular interest to study the thermalization and the mechanism of hadronization of c and b quarks in the QCD medium. In particular, if in Pb–Pb collisions heavy quarks can thermalise and hadronise via recombination with light-flavour quarks present inside the Quark-Gluon Plasma (QGP) or at the QGP phase boundary, the production of charm and beauty baryons is expected to be significantly enhanced (compared to measurements in pp collisions) in the low and intermediate momentum region, say below 10 GeV/ c . An enhancement of the baryon-to-meson ratio was measured in the light-flavour sector (p/π [14] and Λ/K_S^0 [15]) for $1 < p_T < 6$ GeV/ c and can

be described in terms of light-quark recombination and hadron-mass-dependent radial collective flow [14, 15]. A precise measurement in the charm sector would provide crucial information on the charm quark thermalisation and hadronisation in the Quark-Gluon Plasma, as well as on the roles of recombination and radial flow. In addition, such measurements can provide further evidence for the deconfinement of charm quarks in the fireball, see, e.g., [16]. Preliminary measurements by the STAR and ALICE Collaborations indicate a possible enhancement of the ratio Λ_c/D^0 in nucleus–nucleus collisions, but are limited only to high p_T (e.g. $> 6 \text{ GeV}/c$ for ALICE) and still have poor statistical precision [17, 18].

From the experimental point of view, the main issue for the measurement of charmed baryons is their rather short lifetime: the $c\tau$ of the Λ_c is about $59 \mu\text{m}$, a factor of 2 smaller than that of the D^0 meson. In addition, unlike the D^0 , the Λ_c does not have two-prong decays into charged hadrons. The most convenient decay channels are $\Lambda_c^+ \rightarrow p K^- \pi^+$, which has a large three-prong combinatorial background, and $\Lambda_c^+ \rightarrow p K_S^0$, for which a precise determination of the decay vertex is not possible because of the long decay length of the neutral kaon. The former is the benchmark channel considered in the ITS2 TDR [1] and for the ITS3 Inner Barrel upgrade, as described in the following. The measurement requires very precise tracking and impact parameter resolution, because the decay tracks are typically displaced from the main interaction vertex by only a few tens of microns ($\sim c\tau$). This makes the measurement of the Λ_c a powerful benchmark to generally assess the improvement provided by the ITS3 in terms of physics performance for heavy-flavour physics.

The performance studies carried out for the ITS2 are described in detail in [1]. The studies have been repeated for the ITS3 layout using the so-called *hybrid* method, which is also described in [1]: the track parameters in the full-simulation Pb–Pb production with ITS2 geometry have been corrected to mimic the ITS3 impact parameter and momentum resolutions shown in Figs. 10 and 11. It has already been demonstrated for the case of the ITS2 that the method accurately reproduces the full simulation results [1]. In [1], the ITS2 results were presented for the 0–20 % centrality class, using a large p_T interval at low p_T (2 to $4 \text{ GeV}/c$). The improved performance with ITS3 gives access to the 0–10 % centrality class, where the physics effects are expected to be larger, and to measurements in narrower p_T intervals of $1 \text{ GeV}/c$ (shown in the figure) or even $0.5 \text{ GeV}/c$ at low p_T . The finer p_T binning would largely improve the precision on the spectrum shape and on its comparison to other charm hadron species, which is sensitive to hadronisation mechanisms and to the effect of radial flow. A comparison of the performance with ITS2 (using the new centrality range and p_T binning) and ITS3 is shown in Fig. 12 for the statistical significance $S/\sqrt{S+B}$ (left) and signal-to-background S/B ratio (right). S and B are the signal and background yields in an invariant-mass range of $\pm 3\sigma$ around the Λ_c mass, where σ is the invariant-mass resolution (about 5 to $15 \text{ MeV}/c^2$ depending on p_T). The statistical significance is given for 8 billion events in the 0–10 % centrality class, corresponding to $L_{\text{int}} = 10 \text{ nb}^{-1}$. An improvement is found with ITS3 of a factor about four for the significance and ten for the S/B ratio, because the better pointing resolutions allow for a larger rejection of the combinatorial background and a larger efficiency for the signal selection. In particular, the significance in the lowest interval $2 < p_T < 3 \text{ GeV}/c$, where the baryon-to-meson ratio is maximal for Λ_c/K_S^0 , is marginal with ITS2 ($\sim 20\%$ relative statistical uncertainty) and large with ITS3 ($\sim 4\%$ uncertainty).

If the relative abundance of Λ_c with respect to D mesons is strongly enhanced, as suggested by the preliminary measurements at RHIC and LHC, a precise determination of the p_T -integrated Λ_c production yield will be crucial for the measurement of the total $c\bar{c}$ cross section. The latter

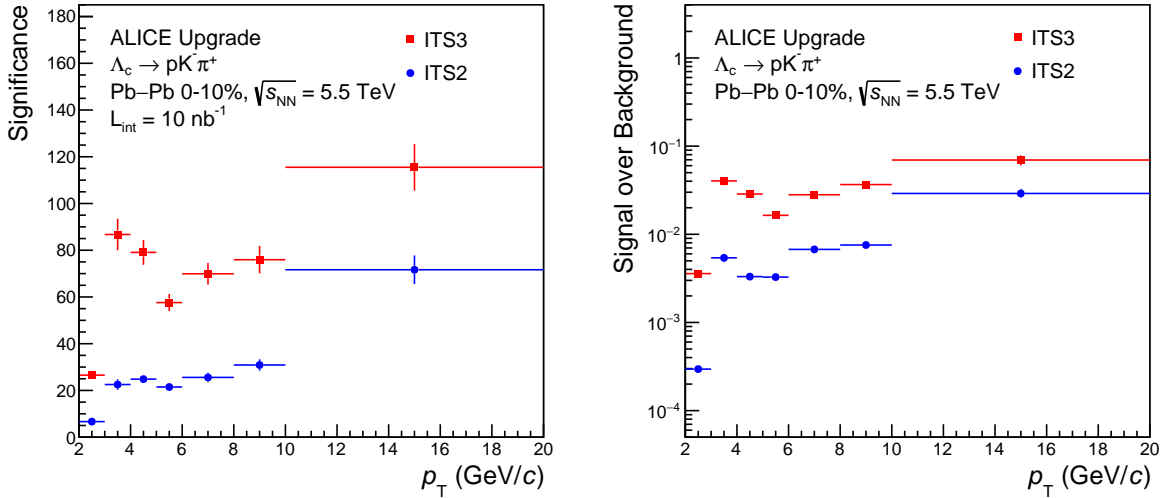


Figure 12: $\Lambda_c^+ \rightarrow p K^- \pi^+$ in central Pb–Pb collisions at $\sqrt{s_{NN}} = 5.5$ TeV ($L_{\text{int}} = 10 \text{ nb}^{-1}$): statistical significance (left) and S/B ratio (right) as a function of p_T .

is an essential input for model calculations of charmonium re-generation in the Quark-Gluon Plasma. Therefore, the large improvement of the significance at low p_T with ITS3 will also impact the quarkonium studies, which are another of the main physics objectives of the ALICE programme after the LS2 upgrade.

5.2 Measurement of Thermal Dielectrons

Electromagnetic radiation produced by the high-temperature system formed in heavy-ion collisions can be detected using real direct photons with very low momentum or virtual photons yielding low invariant-mass dilepton pairs. In this section we discuss the measurement using di-electron pairs in the ALICE central barrel, which requires acceptance for e^+e^- pairs at invariant masses and transverse momenta as low as possible, but at least at $M_{ee} \approx p_{T,ee} \approx T \approx 150$ MeV. This implies electron detection down to $p_T < 100$ MeV/ c . Since the production rate of thermal dileptons is low (suppressed by $\propto \alpha^2$), very good electron identification is mandatory to suppress the combinatorial background in which one of the particles of the pair is a hadron mis-identified as an electron. Moreover, electrons from π^0 Dalitz decays and photon conversions (mainly from $\pi^0 \rightarrow \gamma\gamma$) produce a large combinatorial background. This background can be estimated using "like-sign" pairs of electrons with the same charge, but it nevertheless reduces the statistical significance $S/\sqrt{S+2B}$ of the signal [19, 20, 21]. This calls for low material budget before and of the innermost detection layer and for the capability to reconstruct e^+e^- pairs from photon conversions and Dalitz decays for rejection before the definition of dielectron candidates.

The proposed ITS3 upgrade will enhance the performance of the measurement of the thermal dielectrons with respect to what will be possible with the ITS2 for the following reasons.

- The reduction of the material budget of the beam pipe by 30% and of the first Inner Barrel layer by a factor of about six determines a reduction by a factor of about three of the number of electrons from photon conversions before the first track measurement point.

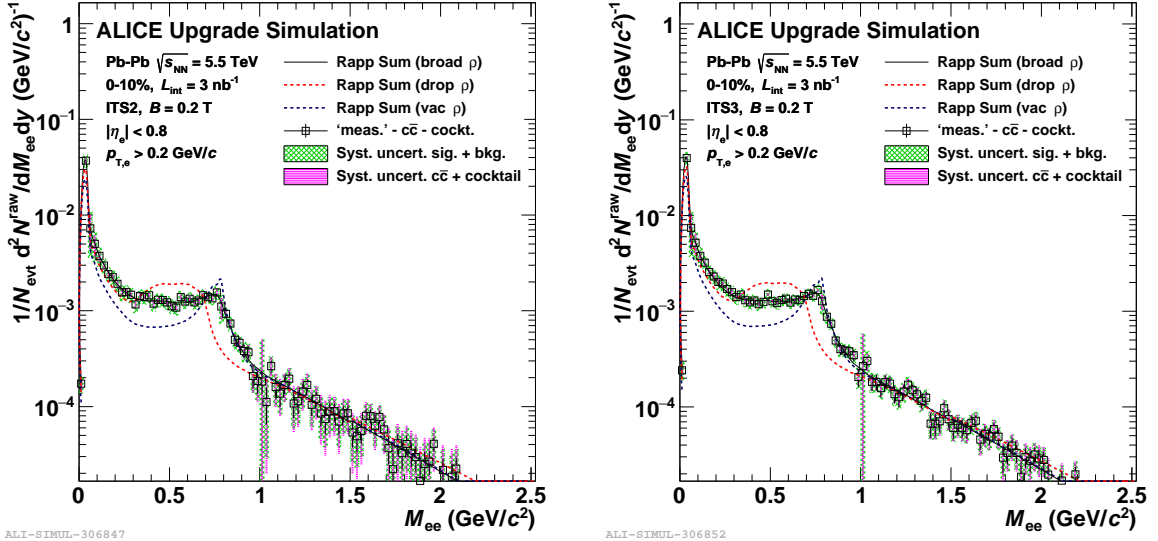


Figure 13: Excess e^+e^- invariant mass spectrum for 0–10 % most central Pb–Pb collisions at $\sqrt{s_{NN}} = 5.5$ TeV, 2.5×10^9 events ($L_{int} = 3 \text{ nb}^{-1}$). The left and right panels refer to the LS2 upgrade (ITS2) and the LS3 upgrade (ITS3) respectively. The green boxes show the systematic uncertainties from the combinatorial background subtraction, the magenta boxes indicate systematic uncertainties related to the subtraction of the cocktail and charm contribution.

- The enhanced low- p_T tracking capability of the ITS3 substantially improves the reconstruction efficiency of photon conversions in which one of the particles of the dielectron pair often has very low momentum. This reduces the combinatorial background.
- The improved pointing resolution of the ITS3 enables efficient tagging of electrons from semi-leptonic charm decays, which form a substantial physical background to the pair-yield and dominate the invariant-mass spectrum at $M_{ee} > 1.1 \text{ GeV}/c^2$. A tight cut on the quadratic sum of the impact parameters of the two electrons reduces the charm background by a factor of about two. This reduces the systematic uncertainties on the thermal excess yield related to the subtraction of the charm contribution.

The dominant sources of systematic uncertainties in the dielectron measurements are the large combinatorial and physical backgrounds. The combinatorial background is estimated and statistically subtracted using the distribution of like-sign pairs from the same event. The latter is corrected for the different detector acceptance for unlike- and like-sign pairs with the correction factor R calculated with mixed-event yields [19, 20, 21]. The systematic uncertainty on R is propagated to the inclusive dilepton signal uncertainty as $\sigma_S/S = \sigma_R/R \cdot (B/S)$. Therefore, the increase of S/B resulting from the reduced conversion probability and the improved conversion rejection with ITS3 determine a linear decrease of the systematic uncertainty. The relative uncertainty on the background σ_R/R was estimated to be 0.02%. An additional systematic uncertainty of 10% is added in quadrature to take into account the track reconstruction and particle identification uncertainties.

In the following, the results of the physics performance study for 2.5 billion central (0–10 %) Pb–Pb collisions at $\sqrt{s_{NN}} = 5.5$ TeV ($L_{int} = 3 \text{ nb}^{-1}$) collected with the solenoid magnetic field at the reduced value of 0.2 T are discussed. The excess e^+e^- invariant-mass spectrum, after subtraction of the combinatorial and charm background, is shown in Fig. 13 for ITS2 (left panel) and ITS3 (right panel). The signal dielectron pairs considered here include thermal radi-

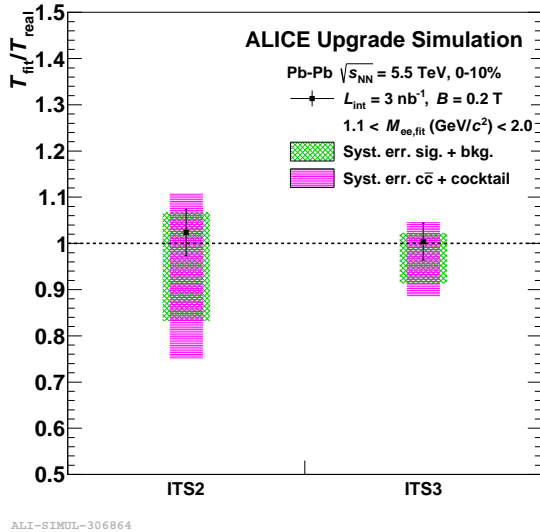


Figure 14: Expected relative uncertainty of the extraction of the T parameter from a fit to the invariant mass excess spectrum in $1.1 < M_{\text{ee}} < 2.0 \text{ GeV}/c^2$ (see text). The results are shown for the ITS2 and ITS3 scenarios, with a tight cut on the quadratic sum of the impact parameters of the lepton pair, and for 0–10 % event centrality. Error bars show the statistical uncertainties. The green boxes show the systematic uncertainties from the combinatorial background subtraction, the magenta boxes indicate systematic uncertainties related to the subtraction of the charm-decay electron contribution.

ation from the QGP and the medium-modified spectral function of the ρ^0 meson. Information on the early temperature of the system can be derived from the invariant-mass dependence of the dilepton yield at masses $M_{\text{ee}} > 1.1 \text{ GeV}/c^2$ where the yield is dominated by the thermal radiation from the QGP if the charm component can be effectively reduced. In order to quantify the sensitivity of the anticipated measurement, an exponential fit to the simulated spectra in the invariant mass region $1.1 < M_{\text{ee}} < 2.0 \text{ GeV}/c^2$ was used. The fit function employed was $dN_{\text{ee}}/dM_{\text{ee}} \propto M_{\text{ee}}^{3/2} \exp(-M_{\text{ee}}/T_{\text{fit}})$. The fit parameter T_{fit} is compared to T_{real} , which is derived from the same fit to the input thermal spectrum. The ratio $T_{\text{fit}}/T_{\text{real}}$ for Pb–Pb collisions in the 0–10 % centrality class is shown in Fig. 14. With respect to the ITS2, the ITS3 upgrade reduces

- the statistical uncertainty by a factor 1.3;
- the systematic uncertainty from the subtraction of the combinatorial background by a factor 2;
- the systematic uncertainty from the subtraction of the light-hadron and charm decay backgrounds by a factor 2.

6 Project Cost Estimate

The project cost estimate is given in Tab. 3. The costs associated to the activities described in the table represent the material costs, excluding institutes' personnel costs and basic infrastructures. These estimates include R&D activities, detector components and production costs as well as industrial or outsourced manpower for production, installation and integration. This represents a first tentative estimate based mostly on the experience of the ongoing developments for the LS2 upgrade. The total cost of the project is estimated to be 5300 kCHF, with about 2000 kCHF for the R&D and 3300 kCHF for the construction. A brief description of the main items of cost is given below.

- **Beampipe.** The development of a beampipe with an inner radius of 16 mm and a wall thickness of 500 μm is estimated to cost about 600 kCHF for the R&D and 900 kCHF for the construction, for a total of about 1500 kCHF.
- **Pixel sensor.** The development of the pixel sensor is the most critical activity. As we have seen in Section 3, this will require the development of three versions with different dimensions. However, owing to the stitching technique, it should be possible to build the three different versions using a single set of fabrication masks. Under this assumption, we estimate the need of two prototyping runs, during the R&D phase, and two runs for the development and production of the final sensor, all based on full-reticle masks. The cost of a full-reticle engineering run with the stitching option is estimated to be of about 350 kCHF for a total of 1400 kCHF. The development of dedicated test systems for the characterization of the sensors in the laboratory, at irradiation facilities and at test beam facilities, will require an additional investment of about 250 kCHF.
- **Thinning and dicing.** The wafer post-processing, in particular the thinning of the wafer to about 30 μm , will also require dedicated R&D. In a first phase, thinning and dicing tests will be carried out using blank wafers. ALPIDE wafers will be used in a second phase of the R&D programme. ALPIDE wafers that have been scrapped because they don't conform to the specifications are very suitable for the development and optimization of the thinning process. In fact, since the ALPIDE wafers have a physical layout that is very similar to the final sensor, they also present very similar mechanical properties. The thinning to such low values will require a planarization of the CMOS wafers and an oxide bonding to a temporary carrier wafer. This development will require a total investment of the order of 500 kCHF.
- **Hybrid printed circuit.** The flexible printed circuit (FPC) board will be based on the CERN's flexible printed circuit technology (EP-DT). The interconnection of the sensor to the FPC using conventional aluminum wedge wire bonding will also be done at CERN (EP-DT bonding lab). This activity is estimated to cost 200 kCHF.
- **Mechanics and Cooling.** The detector mechanical support structures and the tooling for the assembly and installation of the detector will be mostly developed at CERN using the ALICE composite laboratory and the CERN mechanical workshops and metrology service. The development will require a total investment of about 950 kCHF. The cost of the R&D and construction of the cooling system is estimated to be 250 kCHF.
- **Services and patch panels.** The data copper cables and power cables installed during LS2 for the ITS2 should also be suitable for the ITS3. However, the last segment of the services (typical length of about 8 m) and the patch panels in front of the detector

Table 3: Project cost estimate breakdown.

Item	R&D (kCHF)	Construction (kCHF)	Total Cost (kCHF)
Total	2000	3300	5300
Beampipe	600	900	1500
Pixel CMOS Sensors	700	700	1400
Sensor test	100	150	250
Thinning & dicing	200	300	500
Hybrid printed circuit	100	100	200
Mechanics	150	350	500
Assembly & test	50	200	250
Installation tooling	0	200	200
Air cooling	100	150	250
Services	0	100	100
Patch panels	0	150	150

will certainly need to be replaced to match the new mechanical layout. The total cost is estimated to be of the order of 250 kCHF.

- **Readout Electronics and Power Supplies.** The readout and power distribution system that will be installed in LS2 will also be compatible with the ITS3. No additional costs are expected for these systems.

References

- [1] B. Abelev, et al. (ALICE), *Technical Design Report for the Upgrade of the ALICE Inner Tracking System*, Tech. Rep. CERN-LHCC-2013-024, ALICE-TDR-017 (2014), URL <https://cds.cern.ch/record/1625842>
- [2] Z. Ahammed, et al. (ALICE), *Upgrade of the ALICE Time Projection Chamber*, Tech. Rep. CERN-LHCC-2013-020, ALICE-TDR-016 (2014), URL <http://cds.cern.ch/record/1622286/>
- [3] J. Adam, et al. (ALICE), *Addendum to the Technical Design Report for the Upgrade of the ALICE Time Projection Chamber*, Tech. Rep. CERN-LHCC-2015-002, ALICE-TDR-016-ADD-1 (2015), URL <https://cds.cern.ch/record/1984329>
- [4] J. Adam, et al. (ALICE), *Technical Design Report for the Muon Forward Tracker*, Tech. Rep. CERN-LHCC-2015-001, ALICE-TDR-018 (2015), URL <https://cds.cern.ch/record/1981898>
- [5] B. Abelev, et al. (ALICE), *Upgrade of the ALICE Readout & Trigger System*, Tech. Rep. CERN-LHCC-2013-019, ALICE-TDR-015 (2014), URL <https://cds.cern.ch/record/1603472>
- [6] J. Adam, et al., *Technical Design Report for the Upgrade of the Online-Offline Computing System*, Tech. Rep. CERN-LHCC-2015-006, ALICE-TDR-019 (2015), URL <https://cds.cern.ch/record/2011297>
- [7] C. Gargiulo, et al., *Space Frame and Cold Plate Characterization*, Tech. Rep. ALICE ITS Upgrade, Stave EDR, CERN May 2016 (2016), URL <https://indico.cern.ch/event/518710/>
- [8] P. Double, R. Turchetta, *Wafer-scale CMOS X-ray imaging for medical apps*, Tech. rep., EDA Solutions and Rutherford Appleton Laboratory (2012), URL https://www.eetimes.com/document.asp?doc_id=1279813
- [9] P. Yang, et al., *Nucl. Instrum. Meth.* **A785**, 61 (2015)
- [10] D. van den Ende, H. van de Wiel, R. Kusters, et al., *Microelectronics Reliability* **54**, 12, 2860 (2014), URL <http://www.sciencedirect.com/science/article/pii/S0026271414003278>
- [11] A. Straatman, N. Gallego, B. Thompson, et al., *International Journal of Heat and Mass Transfer* **49**, 11, 1991 (2006), URL <http://www.sciencedirect.com/science/article/pii/S0017931006000329>
- [12] D. J. Quade, M. A. Meador, E.-S. Shin, et al., in *Proceedings of the Society for the Advancement of Materials and Process Engineering (SAMPE) Meeting; 17-20 Oct. 2011; Fort Worth, TX; United States* (NASA Glenn Research Center; Cleveland, OH, United States, 2011), URL <https://ntrs.nasa.gov/search.jsp?R=20120000850>
- [13] R. Brun, et al., *GEANT Detector Description and Simulation Tool*, Tech. Rep. CERN Program Library Long Write-up (1994)
- [14] B. Abelev, et al. (ALICE), *Phys. Lett.* **B736**, 196 (2014), <https://arxiv.org/abs/1401.1250>
- [15] B. Abelev, et al. (ALICE), *Phys. Rev. Lett.* **111**, 222301 (2013), <https://arxiv.org/abs/1307.5530>

- [16] A. Andronic, P. Braun-Munzinger, K. Redlich, et al. (2017), <https://arxiv.org/abs/1710.09425>
- [17] S. K. Radhakrishnan (STAR), in *Proceedings of the 27th International Conference on Ultra-Relativistic Nucleus-Nucleus Collisions (Quark Matter 2015): Lido di Venezia, Italy, May 14-17, 2018* (2018), URL <https://indico.cern.ch/event/656452/contributions/2869736/>
- [18] X. Peng (ALICE), in *27th International Conference on Ultrarelativistic Nucleus-Nucleus Collisions (Quark Matter 2018) Venice, Italy, May 14-19, 2018* (2018), 1807.07286
- [19] S. Acharya, et al. (ALICE) (2018), 1807.00923
- [20] S. Acharya, et al. (ALICE) (2018), 1805.04391
- [21] S. Acharya, et al. (ALICE) (2018), 1805.04407